

מכון ויצמן למדע

WEIZMANN INSTITUTE OF SCIENCE



Computationally designed dual-color MRI reporters for noninvasive imaging of transgene expression

Document Version:

Accepted author manuscript (peer-reviewed)

Citation for published version:

Allouche-Arnon, H, Khersonsky, O, Tirukoti, ND, Peleg, Y, Dym, O, Albeck, S, Brandis, A, Mehlman, T, Avram, L, Harris, T, Yadav, NN, Fleishman, SJ & Bar-Shir, A 2022, 'Computationally designed dual-color MRI reporters for noninvasive imaging of transgene expression', *Nature biotechnology*, vol. 40, no. 7, pp. 1143-1149. <https://doi.org/10.1038/s41587-021-01162-5>

Total number of authors:

13

Digital Object Identifier (DOI):

[10.1038/s41587-021-01162-5](https://doi.org/10.1038/s41587-021-01162-5)

Published In:

Nature biotechnology

License:

Other

General rights

@ 2020 This manuscript version is made available under the above license via The Weizmann Institute of Science Open Access Collection is retained by the author(s) and / or other copyright owners and it is a condition of accessing these publications that users recognize and abide by the legal requirements associated with these rights.

How does open access to this work benefit you?

Let us know @ library@weizmann.ac.il

Take down policy

The Weizmann Institute of Science has made every reasonable effort to ensure that Weizmann Institute of Science content complies with copyright restrictions. If you believe that the public display of this file breaches copyright please contact library@weizmann.ac.il providing details, and we will remove access to the work immediately and investigate your claim.



Computationally designed dual-color MRI reporters for noninvasive imaging of transgene expression

Hyla Allouche-Arnon¹, Olga Khersonsky², Nishanth D. Tirukoti¹, Yoav Peleg³, Orly Dym³, Shira Albeck³, Alexander Brandis³, Tevie Mehlman³, Liat Avram⁴, Talia Harris⁴, Nirbhay N. Yadav^{5,6}, Sarel J. Fleishman² and Amnon Bar-Shir¹✉

Imaging of gene-expression patterns in live animals is difficult to achieve with fluorescent proteins because tissues are opaque to visible light. Imaging of transgene expression with magnetic resonance imaging (MRI), which penetrates to deep tissues, has been limited by single reporter visualization capabilities. Moreover, the low-throughput capacity of MRI limits large-scale mutagenesis strategies to improve existing reporters. Here we develop an MRI system, called GeneREFORM, comprising orthogonal reporters for two-color imaging of transgene expression in deep tissues. Starting from two promiscuous deoxyribonucleoside kinases, we computationally designed highly active, orthogonal enzymes ('reporter genes') that specifically phosphorylate two MRI-detectable synthetic deoxyribonucleosides ('reporter probes'). Systemically administered reporter probes exclusively accumulate in cells expressing the designed reporter genes, and their distribution is displayed as pseudo-colored MRI maps based on dynamic proton exchange for noninvasive visualization of transgene expression. We envision that future extensions of GeneREFORM will pave the way to multiplexed deep-tissue mapping of gene expression in live animals.

Genetic engineering of fluorescent reporters has been indispensable for the decryption of biological complexity, and a broad palette of spectrally orthogonal, genetically encoded reporters is in routine use¹. Nonetheless, light absorbance and scattering in live tissues have blocked the application of fluorescent reporters to intact organs and animals, which requires that tissues be subjected to clarification postmortem². Magnetic resonance imaging (MRI) is an attractive alternative to deep-tissue imaging in which noninvasive spatial maps of reporter-gene expression can be overlaid on high-resolution anatomical views of the same subject^{3–11}. Although genetically reconstituted bacterial protein-based gas vesicles were shown to be applicable as polychromatic MRI reporters^{12–14}, and a desired multiplexity might be achieved by combining different MRI methods^{5–7}, most MRI-reporter genes are 'monochromatic'. This lack of orthogonal display capability that is required for simultaneously mapping multiple biological features calls for new strategies for generating spectrally resolved pseudo-color MRI signals of well-synchronized genetically engineered reporters.

In fluorescent imaging, large-scale mutagenesis strategies enable high-throughput selection to produce a desired set of orthogonal reporters¹⁵, but these approaches are inaccessible for MRI due to the low-throughput capabilities of the technique. To overcome this barrier, here we used a computational protein-design methodology to generate genetically engineered reporters for multicolor MRI (GeneREFORM) for simultaneous mapping of orthogonal transgenes. GeneREFORM is composed of MRI-detectable reporter probes (synthetic deoxyribonucleosides, Fig. 1a) that are coupled to computationally designed reporter

genes (deoxyribonucleoside kinases, dNKs, Fig. 1b). The chemical exchange saturation transfer (CEST)^{16,17} contrast mechanism is used for multicolor MRI visualization of reporter probes that are converted by promiscuous multisubstrate dNK enzymes^{18–21} to deoxyribonucleoside-monophosphate (MP) trapping the probes in the cell (Fig. 1c). Using deoxyribonucleoside–dNK pairs in GeneREFORM is an advantage since such pairs display parallel enzymatic activities, similar biodistribution, comparable cellular transport and equivalent accumulation profiles^{22–24}. Important for our purposes, relying on dNK enzymes opens the way to rational mutagenesis to optimize the system^{23,25}.

Results and discussion

Dual-colored MRI-reporter probes. Two major problems preclude the ready use of dNKs to generate 'multicolored' MRI-reporter genes: first, these kinases are highly promiscuous, limiting their ability to generate truly orthogonal probes^{24,26}; and second, they exhibit low-levels of heterologous expression, limiting the production of accumulating probes. To overcome these hurdles, we used a structure- and evolution-based protein-design method, called PROSS²⁷, to design dNK variants that exhibited higher heterologous dNK expression levels without compromising enzymatic activity. PROSS was especially attractive for the development of GeneREFORM because this design method requires the experimental screening of only a few (typically ≤5) designs, thus avoiding the screening bottleneck of MRI-based methods. Next, we rationally designed mutations within the active-site pocket to encode the desired substrate orthogonality.

¹Department of Molecular Chemistry and Materials Science, Weizmann Institute of Science, Rehovot, Israel. ²Department of Biomolecular Sciences, Weizmann Institute of Science, Rehovot, Israel. ³Department of Life Sciences Core Facilities, Weizmann Institute of Science, Rehovot, Israel. ⁴Department of Chemical Research Support, Weizmann Institute of Science, Rehovot, Israel. ⁵Russell H. Morgan Department of Radiology, Johns Hopkins University School of Medicine, Baltimore, MD, USA. ⁶F.M. Kirby Research Center for Functional Brain Imaging, Kennedy Krieger Institute, Baltimore, MD, USA. ✉e-mail: amnon.barshir@weizmann.ac.il

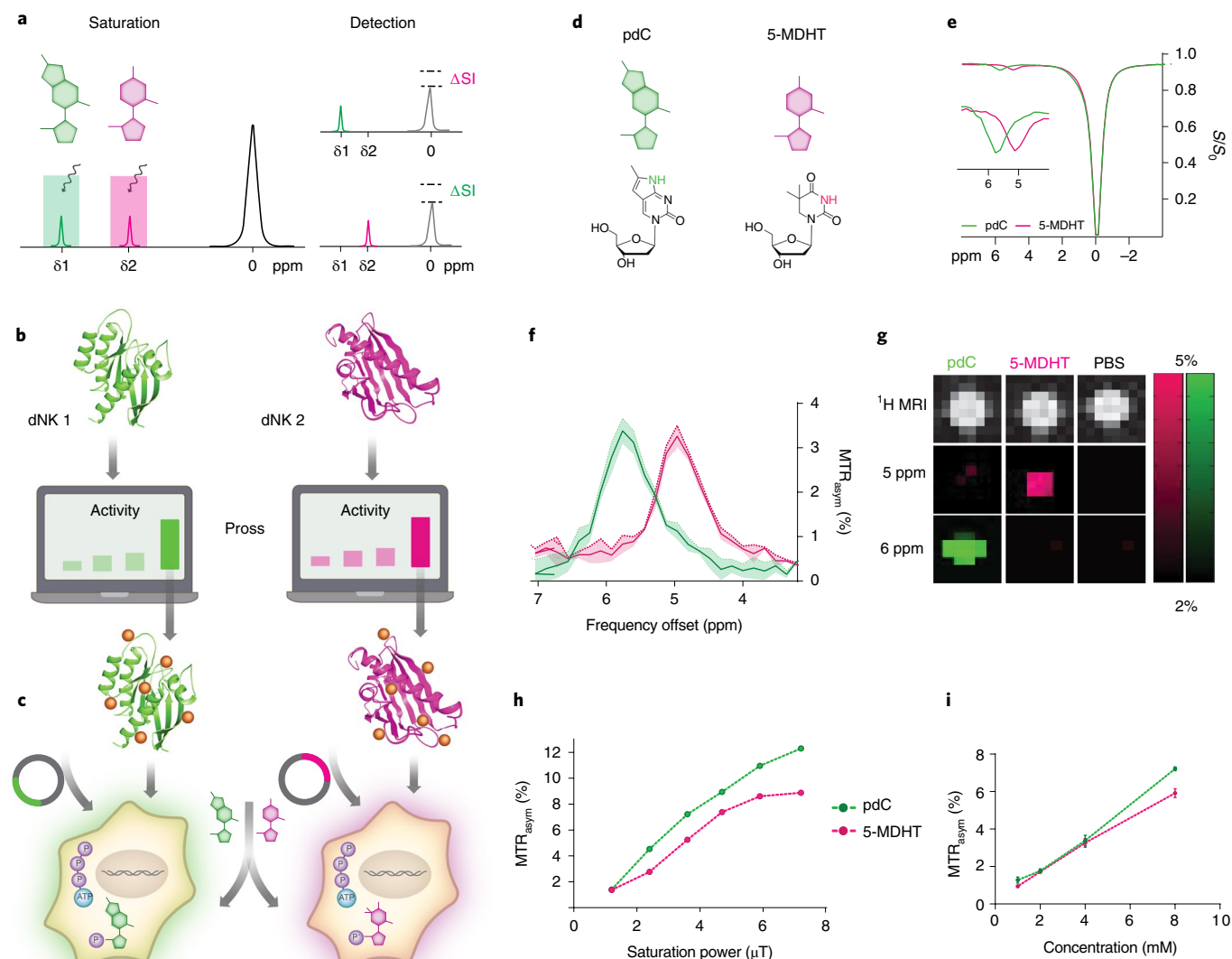


Fig. 1 | MRI pseudocolor reporter system. **a**, The principle of the dual CEST contrast. Applying selective saturation pulses at the frequency of exchangeable protons of synthetic deoxyribonucleosides (δ_1 or δ_2) results in a reduction of the surrounding water signal, ΔSI . **b,c**, Schematic illustration of the dNK1 and dNK2 design (**b**) to obtain a few variants (magenta or green) with enhanced and orthogonal conversion of the deoxyribonucleoside reporter probes to allow their enhanced accumulation in transgene (dNK1 or dNK2)-expressing cells (**c**). **d**, The chemical structure of pdC and 5-MDHT with their -NH exchangeable protons marked in green and magenta, respectively. **e**, Z-spectra of 4 mM 5-MDHT and pdC dissolved in PBS. **f**, MTR_{asym} plots from the data shown in **e** emphasizing the spectral resolution of the obtained CEST profiles. **g**, MTR_{asym} maps of pdC, 5-MDHT and PBS solutions obtained at $\Delta\omega = 5$ and 6 ppm. **h**, MTR_{asym} values of 5-MDHT and pdC solutions (8 mM) as a function of applied saturation powers (μT). **i**, MTR_{asym} values as a function of 5-MDHT (magenta) and pdC (green) concentrations ($n = 3$ independent technical sample). Data were obtained using a 15.2 T MRI scanner. Data are presented as mean values \pm s.e.m.

Two pairs of synthetic deoxyribonucleosides/dNKs were used as a putative reporter probe/reporter gene on which we performed computational design to enhance activity and orthogonality. Specifically, we evaluated the CEST-MRI pseudo-color encoding of 5-methyl-dihydrothymidine and pyrrolo-deoxycytidine (5-MDHT and pdC, respectively Fig. 1d) that were previously paired with the multisubstrate dNK enzymes, herpes simplex virus type 1-thymidine kinase (HSV1-TK)²¹ and *Drosophila melanogaster* dNK (*Dm*-dNK),²⁰ respectively. The resolved z-spectra (Fig. 1e) with the respective MTR_{asym} plots (Fig. 1f) showed negligible signal overlaps at $\Delta\omega$ values of 5 ppm (for 5-MDHT) and 6 ppm (for pdC) enabling their mapping using MRI pseudo-colors (Fig. 1g) of magenta ($\Delta\omega = 5$ ppm) and green ($\Delta\omega = 6$ ppm), with improved spectral resolution compared to polypeptide based CEST colors¹⁶.

In cases where expected concentration ratios are much different to roughly 1:1 of 5-MDHT:pdC, other CEST data processing strategies, such as Lorentzian line fitting of the z-spectra, could be considered to obtain spectrally resolved pseudo-color CEST maps (Supplementary Fig. 1). Plotting the CEST effect of the two probes as a function of the applied saturation pulse (Fig. 1h) and as a function of their concentration (Fig. 1i) showed a similar trend found for these probes at MRI scanners operating at lower magnetic fields^{9,20}. Although the 1-ppm chemical-shift difference between the resonances of the -NH exchangeable protons of 5-MDHT and pdC allows to use them for multicolor CEST-MRI when applied at high magnetic fields ($B_0 = 15.2$ T), their well-resolved CEST peaks should be preserved on more commonly used MRI scanners operating at lower B_0 field strengths (Supplementary Fig. 2).

These results reinforce that 5-MDHT and pdC can be used as deoxyribonucleoside-based reporter probes with spectrally resolved pseudo-color MRI characteristics.

Computation design of MRI-reporter genes. After assigning the CEST signals of pdC and 5-MDHT with MRI pseudo-colors, we used the PROSS protein-stability design algorithm to increase the dNKs' cellular expression levels with the aim of improving the MRI contrast generated by the accumulating deoxyribonucleosides (Fig. 2). Capitalizing on the fluorescence of pdC, which allows us to evaluate its cellular trapping upon phosphorylation by dNK^{20,26}, PROSS was first applied to *Dm*-dNK resulting in seven automatically generated designs from which three were selected for experimental screening in human embryonic kidney-293 (HEK-293) cells (designs d4, d6 and d7, encoding 7, 11 and 15 mutations, respectively; Supplementary Table 1). A significant ($P=0.001$) and more than fivefold higher expression level was found for *Dm*-dNK_7 (Fig. 2a,b) compared to its respective wild-type variant. The improvement in protein-expression levels can be attributed to improved surface polarity, core packing and compatibility of the designed amino acids to the local backbone structure²⁷.

Fluorescence-activated cell sorting (FACS) was then applied to evaluate the cellular accumulation of pdC in wild-type and designed *Dm*-dNK-expressing cells with an expectation that enhanced net uptake of the reporter probe should manifest improved sensitivity of the dNK reporter gene^{23,25}. Representative FACS dot plots clearly showed that pdC accumulation was higher for all three examined *Dm*-dNK mutants compared to wild-type *Dm*-dNK (Fig. 2c), with more than tenfold enhanced accumulation of pdC in live *Dm*-dNK_7-expressing cells (Fig. 2d, $P=0.003$). These data indicate that PROSS resulted in an improved cellular tolerability of *Dm*-dNK_7, as represented by its increased levels of cellular expression, with a larger population of cells accumulating the pdC substrate after its successful conversion.

For GeneREFORM to be applicable in a complex biological milieu, dNK substrate orthogonality is of paramount importance. Therefore, we performed a round of rational single-site mutagenesis of the *Dm*-dNK_7 active site (Supplementary Table 2). Individual mutations at three sites were probed: Gln81 to His, Glu, Val or Ser were engineered to abrogate a hydrogen bond to the natural deoxycytidine (dC), and Ser109 to Ala or Gly and Ala110 to Gly were engineered to allow space for the bulky pyrrolo group (Supplementary Fig. 3). Although the design goal was to improve substrate specificity, we also observed a desirable 2–3-fold improvement in the net uptake of pdC in designs C and D (Gly81Val and Gly81Ser $P=0.007$ and 0.03 , respectively) relative to *Dm*-dNK_7 (Fig. 2e and Supplementary Fig. 4), thus enhancing in cellular catalytic activity when compared to the wild-type *Dm*-dNK.

To examine the designs' substrate specificity (to exclusively phosphorylate pdC), we evaluated their intracellular activity in the presence of their natural competitors, dC and deoxythymidine (dT), as well as the synthetic 5-MDHT (Supplementary Fig. 5). These competition experiments revealed that *Dm*-dNK_7C is preferable (over *Dm*-dNK_7D) showing greater orthogonality and, specifically, 15-fold higher accumulation of pdC when directly comparing it to wild-type *Dm*-dNK (Fig. 2f). The net cellular accumulation of the pdC-MP, which was directly evaluated by liquid chromatography-mass spectrometry (LC-MS), can be enhanced even more when inducing higher expression levels of *Dm*-dNK_7C (Fig. 2g, Supplementary Fig. 6 and Supplementary Table 3), with minimal phosphorylation of supplied natural deoxyribonucleosides (dC and dT, Supplementary Table 3). Nevertheless, at very high expression levels of *Dm*-dNK_7C, other factors (for example, nucleoside transporter efficiency, cellular deoxyribonucleosides availability, phosphorylation of competitive substrates and more) could taper the increase in the accumulated phosphorylated reporter probe.

To evaluate the accuracy of the design campaign, we determined the crystal structure of *Dm*-dNK_7C (Fig. 2h, Supplementary Fig. 7 and Supplementary Table 7. Shown is a monomer unit of the obtained dimeric structure). Overall, the experimental structure is an excellent match to that of the parental enzyme (Protein Data Bank (PDB) 2VP4), which served as the template for the design, exhibiting <0.7 Å root-mean-square deviation across the entire backbone relative to the wild-type structure despite 15 surface mutations (Supplementary Fig. 8). The desired pdC specificity was encoded, as designed, by eliminating a key hydrogen bond between the native substrate dC and Gln81 through a mutation to Val (Supplementary Fig. 9). Furthermore, this mutation likely also enhances pdC binding and thus catalytic efficiency by exploiting the relatively large size of the pyrrole ring of pdC (Fig. 2i). Thus, *Dm*-dNK_7C was found to be the optimal design for pdC conversion, showing increased activity (15-fold higher than the wild-type *Dm*-dNK, Fig. 2f), the desired orthogonality (its activity is not hampered by 5-MDHT, dC or dT, Supplementary Table 3) and an atomically accurate design (Supplementary Fig. 8).

Adopting the same rationale used in designing *Dm*-dNK_7C (Fig. 2a–i), three PROSS-HSV1-TK designs (h3, h6 and h7 in Supplementary Table 4) were expressed in HEK-293 cells (Fig. 2j). HSV1-TK_7, exhibiting 20 mutations, showed a more than sixfold increase in expression levels compared to the wild-type HSV1-TK (Fig. 2k, $P=0.046$). To further improve the specificity and orthogonality of HSV1-TK_7 for 5-MDHT, single-point mutagenesis was performed in the protein active site (Supplementary Table 5). Note that 5-MDHT is not fluorescent and PROSS-designed HSV1-TKs were evaluated using nuclear magnetic resonance (NMR), which is only applicable for very low-throughput practices (compared to FACS-based evaluation, Fig. 2c–f). NMR studies of the intracellular content of cells expressing HSV1-TK mutants incubated with 5-MDHT were performed to evaluate its cellular accumulation (Supplementary Fig. 10) revealing more than tenfold enhanced activity (Fig. 2l, $P=0.03$) in cells expressing HSV1-TK_7B (Tyr87Phe) when compared to nontransfected cells. Here too, much higher net intracellular accumulation of 5-MDHT-MP, which was evaluated directly by LC-MS, could be achieved at higher levels of expression of HSV1-TK_7B (Fig. 2m) with undetectable levels of pdC-MP (by both FACS and LC-MS, Supplementary Fig. 6 and Supplementary Table 6) reflecting the design's orthogonality. In contrast to *Dm*-dNK_7C, however, higher levels of HSV1-TK_7B could also convert dC and dT when supplied at high concentrations (0.5 mM, Supplementary Table 6). Such an improvement in 5-MDHT conversion efficiency and obtained orthogonality (Supplementary Fig. 11 and Supplementary Table 6) can be attributed to the combination of protein surface optimization (PROSS, Figs. 2j,k) and the single-site mutation, Tyr87Phe (Fig. 2o), which allows better accommodation of the bulkier 5-MDHT (Fig. 2l and Supplementary Figs. 12 and 13). Thus, to establish GeneREFORM, we screened only 16 mutants (*Dm*-dNK + HSV1-TK) yet obtained two highly active and highly orthogonal pairs (pdC/*Dm*-dNK_7C and 5-MDHT/HSV1-TK_7B).

Dual-color MRI mapping of transgenes expression. Next, we evaluated the ability to use GeneREFORM to map the simultaneous expression of transgenes with MRI (Fig. 3). The reporter genes were first fused to fluorescent reporters to obtain HSV1-TK_7B-mCherry or *Dm*-dNK_7C-green fluorescent protein (GFP) and stably expressed in Chinese hamster ovary (CHO) cancer cells. Examining the biological tolerance of the obtained stable CHO^{HSV1-TK_7B-mCherry} and CHO^{*Dm*-dNK_7C-GFP} cell lines (Fig. 3a), which orthogonally accumulate pdC or 5-MDHT (Fig. 3b), did not show a notable effect of the dNKs' expression as well as of the subsequent incubation with the synthetic deoxyribonucleosides on cell viability (Supplementary Fig. 14). Nevertheless, further studies may be needed to examine the

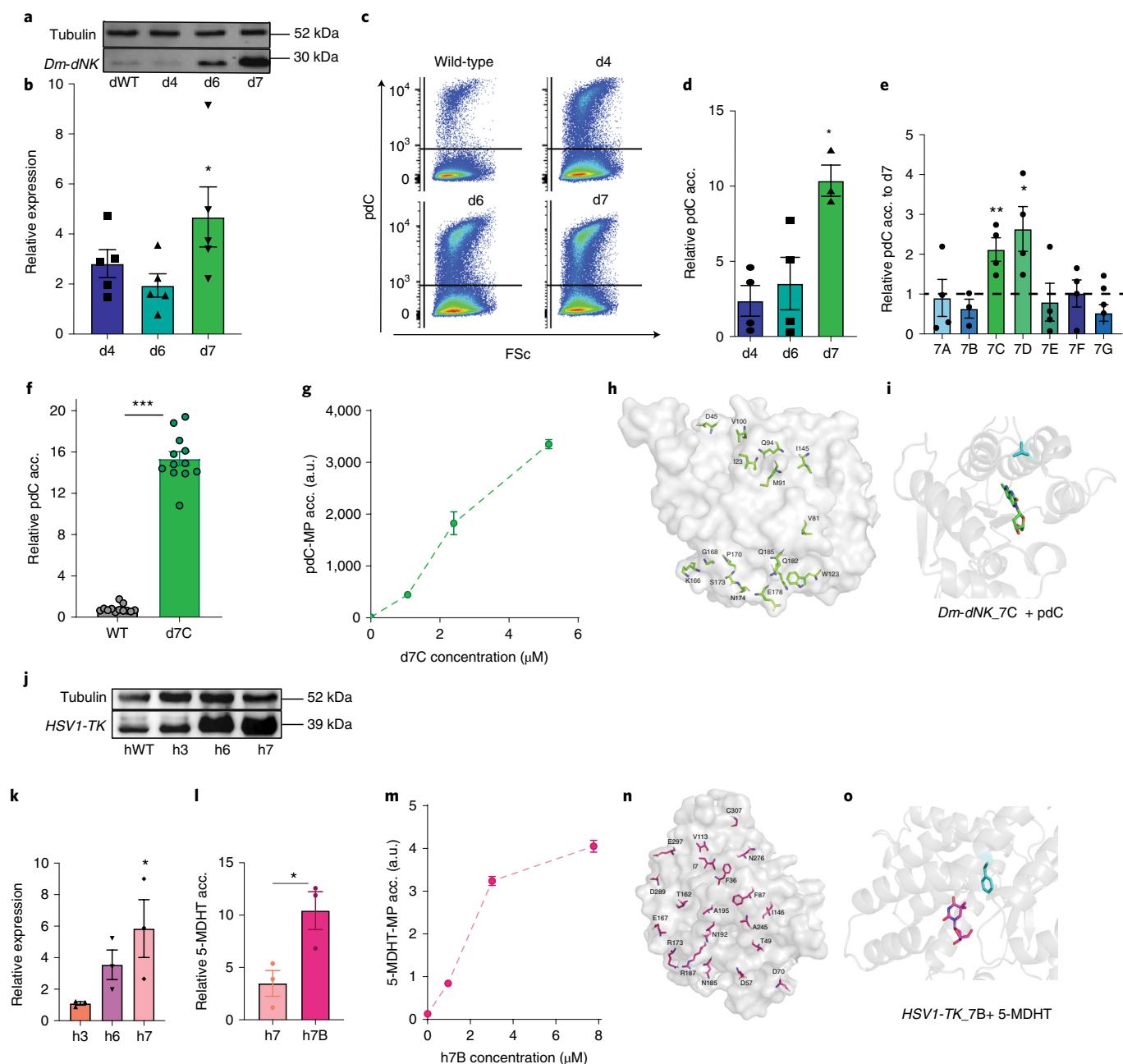


Fig. 2 | Design of highly active and orthogonal *Dm-dNK* and *HSV1-TK* reporter genes. **a**, Representative western blot of wild-type *Dm-dNK* (dWT) and *Dm-dNK* PROSS designs (d4, d6 and d7). **b**, Quantification of protein-expression levels (relative to dWT) of PROSS designs d4, d6 and d7 ($n = 5$ biologically independent samples, $P = 0.01$). **c,d**, Representative FACS scatterplots of HEK-293 cells expressing wild-type *Dm-dNK* and the PROSS designs incubated with pdC (**c**) and FACS data quantification (**d**) ($n = 4$ biologically independent experiments, $P = 0.003$) for assessment of the pdC accumulation (normalized to its accumulation in dWT-expressing cells). **e**, FACS data quantification of pdC accumulation in cells expressing mutants *Dm-dNK_7A-7G* (Supplementary Table 2) normalized to its accumulation in d7-expressing (dashed-line, $n = 4$ biologically independent experiments, for d7C $p = 0.007$ and for d7D $P = 0.03$). **f**, Quantification of FACS data of the pdC accumulation in cells expressing wild-type *Dm-dNK* (dWT) versus its accumulation in *Dm-dNK_7C* (d7C) expressing cells ($n = 12$ biologically independent experiments, $P = 3.43 \times 10^{-16}$). **g**, Cellular content of pdC-MP (evaluated by LC-MS) as a function of *Dm-dNK_7C* cellular concentration ($n = 3$ biologically independent experiments). **h**, A monomer unit representation of the crystal structure of the dimeric *Dm-dNK_7C* presenting its mutations (PDB 6YBH). **i**, Active-site vicinity of *Dm-dNK_7C* (Gln81Val) with pdC. **j**, Representative western blot of wild-type *HSV1-TK* (hWT) and the *HSV1-TK* PROSS designs (h3, h6 and h7). **k**, Quantification of protein-expression levels (relative to hWT) of h3, h6 and h7 ($n = 3$ biologically independent experiments, $P = 0.046$). **l**, Quantification of NMR data of 5-MDHT accumulation in HEK-293 cells expressing *HSV1-TK_7* and *HSV1-TK_7B*, normalized to their accumulation in nontransfected (NT) cells (Supplementary Fig. 10, $n = 3$ biologically independent experiments, $P = 0.03$). **m**, Cellular content of 5-MDHT-MP (evaluated by LC-MS) as a function of *HSV1-TK_7B* cellular concentration ($n = 3$ biologically independent experiments). **n**, *HSV1-TK_7B* structure presenting its mutations (computational model). **o**, Active-site vicinity of *HSV1-TK_7B* with 5-MDHT docked in close proximity to Phe87. Quantitative comparisons of western blots (**b** and **k**) were performed on samples derived from the same experiment and were processed in parallel. Data are presented as mean values \pm s.e.m. Statistics: two-tailed unpaired Student's t -test with $*P < 0.05$ and $**P < 0.01$, $***P < 0.005$. a.u., arbitrary units.

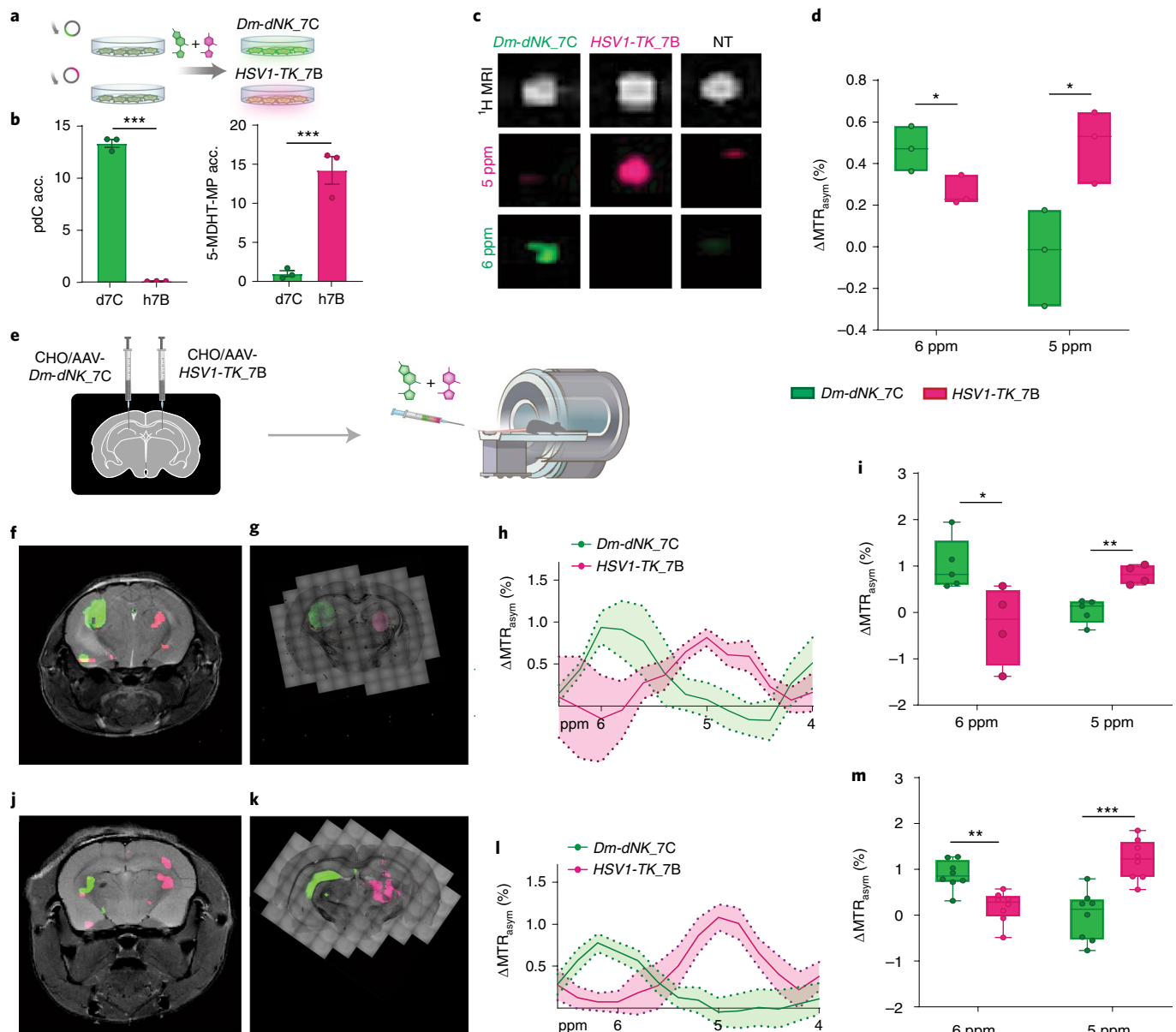


Fig. 3 | In vitro and in vivo MRI of GeneREFORM. **a**, Schematic presentation of the in vitro study. **b**, Relative accumulation of pdC (relative to its accumulation (acc.) in CHO^{HSV1-TK_7B}, determined by FACS $n=3$ biological independent experiments, $P=4.1 \times 10^{-6}$) and 5-MDHT-MP (relative to its accumulation in CHO^{Dm-dNK_7C}, determined by LC-MS, $n=3$ technical replicates $P=0.002$) in CHO cells stably express HSV1-TK_7B-mCherry (h7B) or Dm-dNK_7C-GFP (d7C). **c**, ¹H-MRI, and CEST maps ($\Delta\omega=5$ and 6 ppm) of lysates of cells incubated with mixture of pdC and 5-MDHT. **d**, Quantification of the MTR_{asy} values obtained at $\Delta\omega=5$ and 6 ppm for CHO^{HSV1-TK_7B-mCherry} and CHO^{Dm-dNK_7C-GFP} ($n=3$ technical replicates, $P=0.049$ at 6 ppm and, $P=0.03$ at 5 ppm). **e**, Schematic illustration of the performed in vivo study. **f, j**, The pseudo-colored CEST maps of implanted tumors (**f**) and AAV-infected brain (**j**) represented as ΔMTR_{asy} maps ($MTR_{asy, postinjection} - MTR_{asy, pre-injection}$) obtained at $\Delta\omega=5$ ppm (magenta) and $\Delta\omega=6$ ppm (green) overlaid on anatomical MRI. **g, k**, The corresponding fluorescent images of brain sections of the same scanned mice: tumor (**g**) and AAV infection (**k**), showing the expression of Dm-dNK_7C-GFP (green) and HSV1-TK_7B-mCherry (magenta). **h, l**, Averaged ΔMTR_{asy} plots detected from the regions of interest of CHO^{HSV1-TK_7B-mCherry} and CHO^{Dm-dNK_7C-GFP} ($n=6$ independent animals with bilateral tumors, CHO^{HSV1-TK_7B-mCherry} and CHO^{Dm-dNK_7C-GFP}). Three mice injected with a mixture of 5-MDHT and pdC, two injected with pdC only and one injected with 5-MDHT only). **i, m**, Quantification of the ΔMTR_{asy} values ($\Delta\omega=5$ and 6 ppm) obtained for the tumor model (**i**) ($P=0.03$ at 6 ppm and, $P=0.002$ at 5 ppm) and AAV model (**m**) ($n=8$ biologically independent animals, $P=0.001$ at 6 ppm and $P=0.0002$ at 5 ppm). Adjustments of individual color channels in the fluorescent images (GFP or mCherry) were individually performed. Data are presented as mean values \pm s.e.m. The boxplots in **d, i** and **m** show the median MTR_{asy} value, first and third quartiles as a box, and the whiskers indicate minimum and maximum obtained values. Statistics: unpaired two-tailed Student's t -test with $*P < 0.05$, $**P < 0.01$, $***P < 0.005$.

tolerance of other biological systems to GeneREFORM in extended timeframes. Each cell type was then incubated with a mixture of pdC and 5-MDHT followed by examination of the CEST-MRI characteristics of the intracellular content. A clear and significant difference

was obtained in the CEST maps of lysates of CHO^{HSV1-TK_7B-mCherry} and CHO^{Dm-dNK_7C-GFP} (Fig. 3c,d) at the expected chemical-shift off-sets, which were assigned to magenta ($\Delta\omega=5$ ppm, $P=0.049$) and green ($\Delta\omega=6$ ppm, $P=0.03$) CEST pseudo-colors.

We next evaluated the in vivo performance of GeneREFORM by applying it in two animal models (schematically represented in Fig. 3e). First, 7 days after intracranial injection of CHO^{Dm-dNK_7C-GFP} and CHO^{HSV1-TK_7B-mCherry} cells, two CEST-MRI datasets were acquired before and after intravenous administration of a solution containing a mixture of 5-MDHT and pdC. Subtracting the MTR_{asym} maps (at $\Delta\omega=5$ and $\Delta\omega=6$ ppm) obtained 1 h after the injection of the probes mixture from those obtained before the injection resulted in a pseudo-colored CEST map (1 mm thickness), which was then overlaid on anatomical MRI (Fig. 3f). A fluorescent image of 40- μ m cryogenic section of the brain of the same scanned mouse (Fig. 3g) shows the good correlation between the fluorescent signals of the expressed reporter genes and the MRI pseudo-colors of GeneREFORM. Moreover, intravenous injection of a single probe, either 5-MDHT or pdC, showed accumulation only in one of the two tumors, CHO^{HSV1-TK_7B-mCherry} or CHO^{Dm-dNK_7C-GFP}, respectively, underlying, yet again, the specificity of the designed GeneREFORM platform (Supplementary Fig. 15). The colored CEST signals are shown mostly in the expected tumor region but false-positive CEST contrast may be found in some nontumoral regions. This could be attributed to the fact that pseudo-color CEST maps are generated from two datasets (before and after probes injection), which are very sensitive to prolonged acquisition times that may be accompanied by motion artifacts and compromised signal-to-noise ratio. If applied in organs other than the brain, where the subject's motion is expected to affect the quality of the data, respiratory and electrocardiogram gating should be used²⁸ and faster CEST schemes²⁹ as well as advanced postprocessing protocols³⁰ might be considered to reduce uncertainty and improve GeneREFORM performances in the future. Nevertheless, exclusively for GeneREFORM and in contrast to other MRI-based approaches, the two artificial colors are spectrally resolved showing typical CEST-profile separations (Fig. 3h and Supplementary Fig. 16) with minimum overlap signals at the expected frequencies ($\Delta\omega=6$ ppm and $\Delta\omega=5$ ppm) of accumulated synthetic deoxyribonucleosides even after their systemic administration as a mixture (Fig. 3i, $P=0.03$ at $\Delta\omega=6$ ppm and $P=0.002$ at $\Delta\omega=5$ ppm). These data confirm that GeneREFORM can be applied in vivo to differentiate between two populations of cells expressing different dNKs in a tumor model that is commonly used to demonstrate engineered reporters (Supplementary Table 8) with high density of transgenic cells (45,000–65,000 dNK-expressing cells per MRI voxel, Supplementary Fig. 17) and probe accessibility (through leaky vessels in tumor tissues).

Finally, we extended GeneREFORM to a nontumor setting, where the engineered dNKs are delivered to the mouse brain using a viral vector. Such a setting is expected to exhibit a lower number of transgenic cells per MRI voxel and lower probe accessibility due to the blood–brain barrier and heterogenous tissue distribution. To this end, adeno-associated virus (AAV) vectors carrying either *Dm-dNK_7C-GFP* or *HSV1-TK_7B-mCherry* were first constructed. Two weeks after intracranial injection of AAV^{Dm-dNK_7C-GFP} and AAV^{HSV1-TK_7B-mCherry} a baseline CEST dataset was acquired followed by a continuous infusion of the reporter probes mixture and a subsequent CEST acquisition. Note that in contrast to the bolus injection of the probe mixture into the tumor model (Fig. 3f–i, 150 mg kg^{−1}), continuous infusion of the pdC and 5-MDHT mixture (300 mg kg^{−1} in total) was required here for the sufficient accumulation of each of the probes in the cells expressing their paired transgene. The obtained pseudo-color Δ MTR_{asym} map (1 mm thickness) with a fluorescent image of a brain section from a corresponding region (40 μ m thickness) reflects the applicability of GeneREFORM in a nontumor model (Fig. 3j–m). Although smaller regions of positive CEST signals were found when compared to the fluorescence signals, quantifying the density of HSV1-TK_7B-mCherry and *Dm-dNK_7C-GFP* expressing cells in these regions revealed a range of only 5,500–6,500 dNK-positive cells at each MRI

voxel (Supplementary Fig. 18), thus reflecting the sensitivity of GeneREFORM when comparing it to other MRI reporters (Supplementary Table 8). These relatively high Δ MTR_{asym} values (for roughly 6,000 dNK-positive cells per MRI voxel), compared to the CHO tumor model, might be related to the different expression levels in the two models (Supplementary Fig. 19), the different strategy of probe delivery (infusion versus bolus injection) or the variable levels of cellular nucleoside transporters in different organs. Here again, although continuous probe infusion was required to obtain pseudo-colored maps (Fig. 3j and Supplementary Fig. 20), the uniqueness of GeneREFORM is reflected by the well-resolved CEST peaks of pdC and 5-MDHT (Fig. 3l and Supplementary Fig. 21) although they were delivered systemically at equal concentrations and accumulated only in regions expressing *Dm-dNK_7C* and *HSV1-TK_7B*, respectively (Fig. 3m, $P=0.001$ at $\Delta\omega=6$ ppm and $P=0.0002$ at $\Delta\omega=5$ ppm). These frequency-resolved datasets (Figs. 1f and 3h,l) make CEST-based multiplexed imaging a one-of-a-kind approach with a frequency encodability and spectral features that are lacking in relaxation, susceptibility and diffusion-based contrast mechanisms (Supplementary Table 8).

In summary, we demonstrated the development and implementation of a genetically encoded reporter system GeneREFORM that is not based on luminescence and enables mapping transgene expression in a pseudo-multicolor fashion, noninvasively. We envision that the ability to map several transgenes that are simultaneously expressed using MRI could be combined with other capabilities of this technique, such as mapping connectivity³¹, hemodynamic-related functionality³², neurotransmitter signaling³³ and metabolic pathways³⁴ as a single platform with which to study biological complexity at anatomical, cellular and molecular levels. Our work demonstrates that computational protein-design methods can be applied to systems that are recalcitrant to conventional high-throughput screening to generate highly desirable properties. This strategy can be applied to further enrich the GeneREFORM palette with additional ‘colors’ thereby extending the ‘multicolor’ imaging toolbox to thus far inaccessible deep tissues in live subjects.

Online content

Any methods, additional references, Nature Research reporting summaries, source data, extended data, supplementary information, acknowledgements, peer review information; details of author contributions and competing interests; and statements of data and code availability are available at <https://doi.org/10.1038/s41587-021-01162-5>.

Received: 7 July 2020; Accepted: 12 November 2021;

Published online: 31 January 2022

References

1. Tsiern, R. Y. Constructing and exploiting the fluorescent protein paintbox (Nobel Lecture). *Angew. Chem. Int. Ed. Engl.* **48**, 5612–5626 (2009).
2. Chung, K. et al. Structural and molecular interrogation of intact biological systems. *Nature* **497**, 332–337 (2013).
3. Genove, G., DeMarco, U., Xu, H., Goins, W. F. & Ahrens, E. T. A new transgene reporter for in vivo magnetic resonance imaging. *Nat. Med.* **11**, 450–454 (2005).
4. Cohen, B. et al. MRI detection of transcriptional regulation of gene expression in transgenic mice. *Nat. Med.* **13**, 498–503 (2007).
5. Schilling, F. et al. MRI measurements of reporter-mediated increases in transmembrane water exchange enable detection of a gene reporter. *Nat. Biotechnol.* **35**, 75–80 (2017).
6. Mukherjee, A., Wu, D., Davis, H. C. & Shapiro, M. G. Non-invasive imaging using reporter genes altering cellular water permeability. *Nat. Commun.* **7**, 13891 (2016).
7. Gilad, A. A. et al. Artificial reporter gene providing MRI contrast based on proton exchange. *Nat. Biotechnol.* **25**, 217–219 (2007).
8. Patrick, P. S. et al. Dual-modality gene reporter for in vivo imaging. *Proc. Natl Acad. Sci. USA* **111**, 415–420 (2014).

9. Bar-Shir, A. et al. Transforming thymidine into a magnetic resonance imaging probe for monitoring gene expression. *J. Am. Chem. Soc.* **135**, 1617–1624 (2013).
10. Bartelle, B. B., Szulc, K. U., Suero-Abreu, G. A., Rodriguez, J. J. & Turnbull, D. H. Divalent metal transporter, DMT1: a novel MRI reporter protein. *Magn. Reson. Med.* **70**, 842–850 (2013).
11. Tannous, B. A. et al. Metabolic biotinylation of cell surface receptors for in vivo imaging. *Nat. Methods* **3**, 391–396 (2006).
12. Lu, G. J. et al. Acoustically modulated magnetic resonance imaging of gas-filled protein nanostructures. *Nat. Mater.* **17**, 456–463 (2018).
13. Mizushima, R. et al. Multiplexed (129)Xe HyperCEST MRI detection of genetically reconstituted bacterial protein nanoparticles in human cancer cells. *Contrast Media Mol. Imaging* **2020**, 5425934 (2020).
14. Shapiro, M. G. et al. Genetically encoded reporters for hyperpolarized xenon magnetic resonance imaging. *Nat. Chem.* **6**, 629–634 (2014).
15. Shaner, N. C. et al. Improved monomeric red, orange and yellow fluorescent proteins derived from *Discosoma* sp. red fluorescent protein. *Nat. Biotechnol.* **22**, 1567–1572 (2004).
16. McMahon, M. T. et al. New ‘multicolor’ polypeptide diamagnetic chemical exchange saturation transfer (DIACEST) contrast agents for MRI. *Magn. Reson. Med.* **60**, 803–812 (2008).
17. Liu, G. et al. In vivo multicolor molecular MR imaging using diamagnetic chemical exchange saturation transfer liposomes. *Magn. Reson. Med.* **67**, 1106–1113 (2012).
18. Johansson, M., van Rompay, A. R., Degreve, B., Balzarini, J. & Karlsson, A. Cloning and characterization of the multisubstrate deoxyribonucleoside kinase of *Drosophila melanogaster*. *J. Biol. Chem.* **274**, 23814–23819 (1999).
19. Black, M. E., Newcomb, T. G., Wilson, H. M. & Loeb, L. A. Creation of drug-specific herpes simplex virus type 1 thymidine kinase mutants for gene therapy. *Proc. Natl Acad. Sci. USA* **93**, 3525–3529 (1996).
20. Bar-Shir, A. et al. Quantification and tracking of genetically engineered dendritic cells for studying immunotherapy. *Magn. Reson. Med.* **79**, 1010–1019 (2018).
21. Bar-Shir, A., Liu, G., Greenberg, M. M., Bulte, J. W. & Gilad, A. A. Synthesis of a probe for monitoring HSV1-*tk* reporter gene expression using chemical exchange saturation transfer MRI. *Nat. Protoc.* **8**, 2380–2391 (2013).
22. Arner, E. S. & Eriksson, S. Mammalian deoxyribonucleoside kinases. *Pharmacol. Ther.* **67**, 155–186 (1995).
23. Gambhir, S. S. et al. A mutant herpes simplex virus type 1 thymidine kinase reporter gene shows improved sensitivity for imaging reporter gene expression with positron emission tomography. *Proc. Natl Acad. Sci. USA* **97**, 2785–2790 (2000).
24. Tjuvajev, J. G. et al. Imaging the expression of transfected genes in vivo. *Cancer Res.* **55**, 6126–6132 (1995).
25. Likar, Y. et al. A new pyrimidine-specific reporter gene: a mutated human deoxycytidine kinase suitable for PET during treatment with acycloguanosine-based cytotoxic drugs. *J. Nucl. Med.* **51**, 1395–1403 (2010).
26. Liu, L., Li, Y., Liotta, D. & Lutz, S. Directed evolution of an orthogonal nucleoside analog kinase via fluorescence-activated cell sorting. *Nucleic Acids Res.* **37**, 4472–4481 (2009).
27. Goldenzweig, A. et al. Automated structure- and sequence-based design of proteins for high bacterial expression and stability. *Mol. Cell* **63**, 337–346 (2016).
28. Meier, S. et al. Non-invasive detection of adeno-associated viral gene transfer using a genetically encoded CEST-MRI reporter gene in the murine heart. *Sci. Rep.* **8**, 4638 (2018).
29. Villano, D. et al. A fast multislice sequence for 3D MRI-CEST pH imaging. *Magn. Reson. Med.* **85**, 1335–1349 (2021).
30. Cohen, O., Huang, S., McMahon, M. T., Rosen, M. S. & Farrar, C. T. Rapid and quantitative chemical exchange saturation transfer (CEST) imaging with magnetic resonance fingerprinting (MRF). *Magn. Reson. Med.* **80**, 2449–2463 (2018).
31. Basser, P. J., Pajevic, S., Pierpaoli, C., Duda, J. & Aldroubi, A. In vivo fiber tractography using DT-MRI data. *Magn. Reson. Med.* **44**, 625–632 (2000).
32. Ogawa, S., Lee, T. M., Kay, A. R. & Tank, D. W. Brain magnetic resonance imaging with contrast dependent on blood oxygenation. *Proc. Natl Acad. Sci. USA* **87**, 9868–9872 (1990).
33. Lee, T., Cai, L. X., Lelyveld, V. S., Hai, A. & Jasanoff, A. Molecular-level functional magnetic resonance imaging of dopaminergic signaling. *Science* **344**, 533–535 (2014).
34. Rodrigues, T. B. et al. Magnetic resonance imaging of tumor glycolysis using hyperpolarized ¹³C-labeled glucose. *Nat. Med.* **20**, 93–97 (2014).

Publisher's note Springer Nature remains neutral with regard to jurisdictional claims in published maps and institutional affiliations.

© The Author(s), under exclusive licence to Springer Nature America, Inc. 2022

Methods

Reporter probes. pDC (Berry and Associates, Inc., catalog no. PYA11090-B010), dC (Chem-Impex, catalog no. 01945) and dT (Chem-Impex, catalog no. 00306) were commercially available. 5-MDHT was synthesized as previously described²¹.

Computational model for dNK mutations. The PROSS jobs for *Dm*-dNK and HSV1-TK were submitted online on the webserver (<http://pross.weizmann.ac.il>), using the PDB file 2VP4 (chain A) for *Dm*-dNK and IKI7 (chain A) for HSV1-TK. The constructs for experimental characterization were chosen so they would have a reasonably high number of mutations and would be sufficiently different from one another. Models of PROSS stabilized variants were obtained from the webserver. The ligands were put into these models by substrate overlay (pair fitting in PyMol v.2.4.0 software) with the substrate present in the crystal structures (DCP in the case of *Dm*-dNK and ID2 in the case of HSV1-TK).

Cloning. pcDNA3.1. *Dm*-dNK (NCBI Gene ID: 42273) and HSV1-TK (NCBI Gene ID: 2703374) genes and PROSS designs were obtained from TWIST Bioscience Ltd. The DNA fragments were subcloned into pcDNA3.1 (Thermo Fisher Scientific, catalog no. V790-20) under the cytomegalovirus promoter and a fused V5-tag. A second cycle of single-site mutations in the active site of HSV1-TK_7 and *Dm*-dNK_7 was obtained using a PCR-guided protocol with a dedicated experimental kit KAPA HiFi HotStart ReadyMix PCR Kit (Hoffmann-La Roche Ltd, catalog no. 07958927001) and appropriate designed primers for mutation insertion. After identifying the preferred mutants, their genes were fused to the genes encoding the fluorescent proteins GFP and mCherry, to obtain pcDNA3.1-*Dm*-dNK_7C-GFP and pcDNA3.1- HSV1-TK_7B-mCherry.

pcDNA4/TO. *Dm*-dNK_7C-GFP and HSV1-TK_7B_mCherry were subcloned into expression vector pcDNA4/TO (T-Rex, Thermo Fisher Scientific, catalog no. V102020) downstream of a doxycycline-regulated cytomegalovirus promoter.

AAV (AAV2/8). The genes encoding *Dm*-dNK_7C-GFP and HSV1-TK_mCherry were cloned into the AAV2/8 viral vector under the CAG promoter by the Neurophotonics Centre (Quebec, Canada) and the constructs AAV^{Dm-dNK_7C-GFP} and AAV^{HSV1-TK_mCherry} were obtained at a titer of 5.9×10^{13} GC per ml and 2.1×10^{13} GC per ml, respectively.

Cells. HEK-293 cells were originally purchased from ATCC, catalog no. CRL-1573 lot no. 1353700 and provided by the tissue culture cell repository unit at the Weizmann Institute of Science. CHO cells were purchased from ATCC, catalog no. CCL-K1).

Transient cell transfection. HEK-293 cells were transiently transfected using the JetPEI transfection reagent (Polyplus transfection, catalog no. 101-10N) according to the manufacturer instructions, with the various HSV1-TK- and *Dm*-dNK-mutated genes cloned in the pcDNA3.1 expression plasmid. Twenty-four hours posttransfection, the cells were used for substrate accumulation studies, using FACS, NMR or LC-MS.

Stable cell-line generation. Cells were transfected with either pcDNA3.1-*Dm*-dNK_7C-GFP or pcDNA3.1- HSV1-TK_7B-mCherry. Forty-eight hours posttransfection, GFP and mCherry positive cells were sorted using a FACS Aria cell sorter (BD Biosciences). Sorted cells were subsequently cultured for additional cycles of selection in the presence of geneticin (G418 Sulfate salt, Thermo Fisher Scientific, catalog no. 11811023) at cell-type-appropriate concentrations (300–700 ng ml⁻¹) to reach at least 90% positive cells expressing *Dm*-dNK_7C-GFP or HSV1-TK_7B-mCherry.

Doxycycline-induced expression. HEK-293 cells were transiently transfected, using the JetPEI transfection reagent (Polyplus transfection, catalog no. 101-10N), with a pcDNA4/TO vector encoding to either *Dm*-dNK_7C-GFP or HSV1-TK_7B_mCherry together with the regulatory plasmid pcDNA6/TR, to control the expression of the reporters under doxycycline. Twenty-four hours posttransfection, the expression of the dNK transgenes was induced by doxycycline (0.001, 0.01 and 0.1 μ g ml⁻¹) for 24 h in a cell-culture medium. The protein expression of *Dm*-dNK_7C-GFP and HSV1-TK_mCherry under various doxycycline concentrations was validated by both fluorescent microscopy or flow cytometry. Protein-expression levels were quantified by western blot analysis using Recombinant multi tag Protein (Biolegend, catalog no. 931301).

Western blot analysis. Cells expressing *Dm*-dNK and HSV1-TK and their mutants were lysed using the RIPA lysis buffer (Merck, catalog no. R0278) according to the manufacturer's instructions. Protein extracts were run on SDS-PAGE and then transferred to a nitrocellulose membrane for western blot analysis. Western blot analyses were performed using anti-V5 antibody (Thermo Fisher Scientific, 1:5,000, catalog no. R960-25) for protein-expression validation and with cellular house-keeping proteins, either anti- β -actin or anti-tubulin antibodies (Santa Cruz Biotechnology Inc., 1:10,000, catalog no. sc-69879, catalog no. sc-5286). HRP conjugated secondary antibodies (goat antimouse: 1:10,000, catalog no.

sc-516102) and signal was revealed by enhanced chemiluminescence substrate EZ-ECL Kit (Biological industries, catalog no. 20-500-120). Binding specificity of all of the antibodies were validated and stated on the manufacturers' websites. The relative expression level of the studied samples was calculated by analyzing the chemiluminescent signal detected with the ChemiDoc Imaging System (Bio-Rad). Western blot data analysis was carried out using FIJI software³⁵. The signals of the expressed transgenes were normalized to those of β -actin or tubulin protein in each sample.

Cloning expression and purification of HSV1-TK_7B and *Dm*-dNK_7C. *Dm*-dNK_7C (1-224 AA) PROSS variant, harboring 16 mutations was cloned into the expression vector pET28-bdSumo. pET28-bdSumo was constructed by transferring the His14-bdSUMO cassette from the expression vector (designated K151) generously obtained from D. Görlich from the Max-Planck Institute, Göttingen, Germany³⁶ into the expression vector pET28-TevH³⁷. Cloning of *Dm*-dNK_7C was performed using the restriction-free method³⁸. For its expression, a 7.5 l of culture of BL21(DE3) was induced with 200 μ M isopropyl- β -D-thiogalactoside and grown at 15 °C overnight. The culture was harvested and lysed by a cool cell disrupter (Constant Systems) in lysis buffer (20 mM Tris pH 7.5, 1 mM DTT, 5 mM MgCl₂, 8% glycerol) containing 200,000 units per 100 ml of lysozyme, 20 μ g ml⁻¹ DNaseI, 1 mM MgCl₂, 1 mM phenylmethylsulfonyl fluoride and protease inhibitor cocktail. After clarification of the soup by centrifugation, 1% Triton X-100 was added to the lysate and incubated for 15 min before incubation with 5 ml washed Ni beads (Adar Biotech) for 1 h at 4 °C. After removing the soup, the beads were washed four times with 50 ml of lysis buffer containing 3 mM ATP. *Dm*-dNK_7C (without tags) eluted from the beads by incubation with 5 ml of cleavage buffer (20 mM Tris pH 7.5, 1 mM DTT, 5 mM MgCl₂, 8% glycerol and 0.4 mg bdSumo protease) for 2 h at room temperature. The soup containing the cleaved *Dm*-dNK_7C was removed and an additional 5 ml of cleavage buffer was added to the beads for 2 h at room temperature. The two elutions were combined, concentrated and applied to a size exclusion column (HiLoad 16/60, Superdex75 prep-grade, GE Healthcare) equilibrated with 20 mM Tris pH 7.5, 1 mM DTT, 5 mM MgCl₂, 8% glycerol. Pure *Dm*-dNK_7C that migrated as a single peak at 65 ml was concentrated to 12 mg ml⁻¹ and was flash frozen in aliquots using liquid nitrogen and stored at –80 °C. For crystallization experiments, pDC was added to the concentrated protein at a final concentration of 5 mM.

FACS in vitro studies. Twenty-four hours following cell transfection with wild-type or mutated *Dm*-dNK or HSV1-TK genes, 1 million cells were incubated (37 °C, 5% CO₂) for 3 h with 300 μ l of culture media containing 1 mM pDC. For competition experiments, a mixture of pDC (1 mM), 5-MDHT (1 mM), dC (0.5 mM) and dT (0.5 mM) was used for incubation. Cells were then washed twice with cold phosphate-buffered saline (PBS), resuspended shortly using 50 μ l of a trypsin A solution (Biological industries, catalog no. 03-050-1B) and then transferred into a PBS solution containing 1% fetal bovine serum. Before the FACS analysis, cells were filtered through a 40- μ m filter to remove cell clumps and debris into dedicated FACS tubes. The accumulation of pDC in the examined cells was detected using a ultraviolet-fluorescent laser setup of $\lambda_{\text{excitation}} = 355$ nm and $\lambda_{\text{emission}} = 460$ nm. All FACS studies were acquired using a LSRII cell analyzer flow cytometer (BD Biosciences) running BD FACSDIVA v.8.0.1 software (BD Biosciences). All data were processed using FlowJo Software v.10 (Tree Star).

LC-MS analysis of deoxyribonucleosides-MP. Twenty-four hours following cell transfection, 1 million cells were incubated with a mixture of pDC (1 mM), 5-MDHT (1 mM), dC (0.5 mM) and dT (0.5 mM) for 3 h. Cells were then washed and lysed and the deoxyribonucleoside-MP content, that is dC-MP, dT-MP, pDC-MP and 5-MDHT-MP, was analyzed using LC-tandem MS, following sample preparation as previously described³⁹. An Acquity I-class ultra-performance liquid chromatography system (Waters) and Xevo TQ-S triple quadrupole mass spectrometer (Waters) equipped with an electrospray ion source and operating in the positive ion mode was used for the analysis of deoxyribonucleosides-MP content. MassLynx and TargetLynx software (v.4.2, Waters) were used to acquire and analyze the data. Briefly, dC-MP, dT-MP and 5-MDHT-MP were detected using multiple reaction monitoring with the following parameters: 308.1 > 80.9 and 308.1 > 111.8 m/z (collision energy 26 and 12 eV, respectively) for dC-MP; 322.9 > 80.8 and 322.9 > 207.1 m/z (collision energy 18 and 6 eV, respectively) for dT-MP; and 339.1 > 81.0 and 339.1 > 223.0 m/z (collision energy 11 and 6 eV, respectively) for 5-MDHT-MP. The absolute concentrations of dC-MP and dT-MP were determined using relevant standard curves and adenosine-¹⁵N₃ 5'-MP as the internal standard (Sigma Aldrich, catalog no. 662658), with 353.1 > 97.0 and 353.1 > 141.1 m/z (collision energy 28 and 20 eV, respectively). The relative concentration of 5-MDHT-MP was analyzed using the proper mass peak area. The relative concentration of pDC-MP was evaluated using the peak area absorption based on the compound's absorbance wavelength, 338 nm.

CEST-MRI of deoxyribonucleoside solutions. 5-MDHT and pDC were dissolved to obtain a range of concentrations (1–8 mM) in PBS (pH 7.2) and placed in 1-mm diameter capillaries located in a horizontal 15.2 T MRI scanner (Biospec, Bruker)

running ParaVision v.6.0.1 software. Once the sample's temperature was stabilized at 37°C, ¹H-magnetic resonance images were obtained using a rapid acquisition with relaxation enhancement (RARE) pulse sequence (TR/TE = 6,000/20 ms, RARE factor 8, 1-mm slice thickness, field of view (FOV) = 16 × 16 mm², matrix size 256 × 256, resolution 0.06 × 0.06 mm², number of averages (NA) = 2). A RARE sequence (TR/TE = 6,000/20 ms, RARE factor 8, 1-mm slice thickness, FOV = 20 × 20 mm², matrix size 64 × 64, resolution 0.3 × 0.3 mm², NA = 2), including a CEST module with a B₁ saturation pulse applied for 4,000 ms at different saturation powers (1.2, 2.4, 3.6, 4.7 or 7.2 μT) with a sweep range from −10 to +10 ppm was used to acquire CEST-weighted images. Voxel-based B₀ correction was performed as described before⁴⁰, using data obtained with the same parameters used for CEST except for TR = 1,500 ms and B₁/t_{sat} = 0.5 μT per 500 ms, with a sweep range from −1 to +1 ppm. CEST data processing was performed as previously described⁴¹, using custom-written scripts in MATLAB (R2014a, Mathworks), which are available through <http://godzilla.kennedykrieger.org/CEST/> and as previously described^{9,20}.

Lorentzian line shape fitting of CEST-MRI data of deoxyribonucleoside solutions. Substrate peaks in the Z-spectra were quantified using multiple-Lorentzian line shape fitting⁴², using the L-BFGS-B function minimization algorithm in Python v.2.7 (ref. 43). To distinguish between pdC and 5-MDHT signals, the frequency offset of the CEST signal was allowed to vary between 4.5 and 6.5 ppm. Peaks with a fitted frequency less than 5.4 ppm were attributed to 5-MDHT and peaks with a fitted frequency greater than 5.4 ppm were attributed to pdC. The peak amplitudes were then plotted based on a voxel-by-voxel basis (Supplementary Fig. 1).

Simulating CEST-MRI of pdC and 5-MDHT at different field strengths. CEST signals at different field strengths were simulated using the Bloch-McConnell equations⁴⁴. The CEST parameters in the simulations matched the experimental parameters (3.6 μT, 4 s continuous wave saturation). The water, pdC and 5-MDHT parameters were as follows. Water T₁ 3.6 s; T₂ 2.2 s; k_{ex} 1 s^{−1}; ω 0 ppm; [H] 111,200 mM. pdC (−OH): T₁ 3.6 s; T₂ 1.0 s; k_{ex} 2,000 s^{−1}; ω 1.0 ppm; [H] 20 mM. pdC (−NH): T₁ 3.6 s; T₂ 1.0 s; k_{ex} 900 s^{−1}; ω 5.8 ppm; [H] 10 mM. 5-MDHT (−OH): T₁ 3.6 s; T₂ 1.0 s; k_{ex} 2,000 s^{−1}; ω 1.0 ppm; [H] 20 mM. 5-MDHT (−NH): T₁ 3.6 s; T₂ 1.0 s; k_{ex} 1,700 s^{−1}; ω 5.0 ppm; [H] 10 mM.

NMR studies for the assessment of 5-MDHT accumulation. Twenty million HEK-293 cells transiently transfected with HSV1-TK variants (7, 7A, 7B or 7C) and nontransfected cells were incubated in a cell-culture media containing 2 mM 5-MDHT and then lysed as described elsewhere⁴⁵. The intracellular content was dissolved in PBS and transferred to 5-mm NMR tubes, followed by high-resolution ¹H-NMR spectroscopy, acquired using a vertical 500 MHz NMR spectrometer (Bruker). ¹H-NMR spectra of the extracts were recorded with a water-suppression pulse sequence to detect the soluble metabolites (100 scans per spectrum). The signal integrals of the typical functional groups of 5-MDHT (methyl groups (−CH₃), at 1.22 ppm and of the CH on the C1' position of the sugar moiety at 6.29 ppm) were determined and relatively quantified.

In vitro CEST-MRI of pdC and 5-MDHT cellular accumulation. Twenty million CHO cells stably expressing either HSV1-TK_7B-mCherry or Dm-dNK_7C-GFP and nontransfected cells were incubated in cell-culture media containing a 2 mM mixture solution of 5-MDHT and pdC. Following 3 h of incubation (37°C, 5% CO₂), the cells were lysed using a dual-phase extraction methodology described elsewhere⁴⁵. The dry content was dissolved in PBS, pH 7.2, and transferred to 1 mm diameter capillaries for MRI studies acquired on a 15.2 T MRI scanner (Biospec, Bruker) running ParaVision v.6.0.1 software, following the same protocol described above for the CEST acquisition for 5-MDHT and pdC solutions.

Animal care. All experiments involving animals were performed following the described experimental protocol approved by the Weizmann Institute of Sciences Animal Care and Use Committee (IACUC approval number 11850319-2). All animals were kept in a daily controlled room at the Weizmann Institute of Sciences animal facility with a surrounding relative humidity level of 50 ± 10% and a temperature of 22 ± 1°C, with a 12/12 cycle of dark and light phases.

CHO tumor inoculations. For the intracranial tumor xenograft model, stable CHO cell lines expressing either HSV1-TK_7B-mCherry or Dm-dNK_7C-GFP were intracranially inoculated (2 × 10⁵ cells per 2 μl of serum-free medium) into the striatum (coordinates 1 mm posterior to Bregman, 2.0 mm lateral to the midline and 3.0 mm ventral to the surface of the skull) of 8-week-old female immunodeficient Hsd:Athymic Nude-Foxn1nu mice (Envigo), which generated intracranial tumors in both hemispheres.

AAV inoculations. AAV^{Dm-dNK_7C-GFP} (5.9 × 10¹³ GC per ml) and AAV^{HSV1-TK_7B-mCherry} (2.1 × 10¹³ GC per ml) were intracranially injected (2 μl in PBS) into two different hemispheres of the brain of 8-week-old female SJL/JCrHsd (Envigo) mice at the following coordinates: 1.5 mm posterior to Bregman, 1.5 mm lateral to the midline and 3.0 mm ventral to the surface of the skull.

In vivo MRI. All in vivo experiments were performed on anesthetized mice (1.5% isoflurane) that were placed in a horizontal 15.2 T preclinical MRI scanner (Biospec, Bruker) equipped with a 23 mm volume radiofrequency coil running ParaVision v.6.0.1 software. Mice were monitored for their breathing throughout the MRI session, using a dedicated respiratory monitor setup. All CEST datasets were acquired following conventional anatomical magnetic resonance images, to assist with locating the mice in the center of the magnet. Anatomical images of the mouse brain were acquired using a RARE pulse sequence (TR/TE = 6,000/20 ms, RARE factor 8, 1 mm slice thickness, FOV = 21 × 21 mm², matrix size 256 × 128, resolution 0.08 × 0.16 mm², NA = 2). CEST-weighted images were acquired with a modified RARE pulse sequence (TR/TE = 6,000/20 ms, RARE factor 16, NA = 1) using a 3.6 μT per 4,000 ms saturation pulse swept from −10 to 10 ppm around the water resonance. Pixel-based B₀ correction was performed using a set of experiments acquired with the same parameters used for acquiring the CEST data except for the followings: TR = 1,500 ms, and a saturation pulse (B₁/t_{sat} = 0.5 μT per 500 ms) swept from −1 to 1 ppm. CEST data were processed using custom-written scripts in MATLAB (R2014a, Mathworks), which are available through <http://godzilla.kennedykrieger.org/CEST/> and as previously described^{9,20}. ΔMTR_{asym} was defined as (MTR_{asym} (postinjection)) − (MTR_{asym} (preinjection)). ΔMTR_{asym} maps at saturation frequencies of 5 and 6 ppm were displayed as magenta and green artificial colors of the accumulated 5-MDHT (in HSV1-TK_7B expressing cells) and pdC (in Dm-dNK_7C expressing cells), respectively. Image processing FIJI software³⁵ was used to overlay the two ΔMTR_{asym} maps on an anatomical ¹H-magnetic resonance image for spatial display of the detected CEST signal in a multicolor manner.

In vivo CEST-MRI of brain tumors. Seven days after cell transplantation, full CEST datasets were acquired for each animal before and 1 h following the intravenous injection of a solution containing a mixture of 5-MDHT and pdC (200 μl in saline, 150 mg kg^{−1}). CEST-weighted images were acquired with 1 mm slice thickness, a FOV = 16 × 16 mm² and a matrix size 64 × 64, yielding a spatial resolution of 0.25 × 0.25 mm².

In vivo CEST-MRI of AAV model. Fourteen days after AAV injection, full CEST datasets were acquired for each animal before and after the intravenous delivery of a solution containing a mixture of 5-MDHT and pdC. The injection entailed a bolus of 100 μl (75 mg kg^{−1}) probe mixture followed by a continuous infusion (5 μl min^{−1}) of the probe mixture over 1 h (225 mg kg^{−1}). CEST-weighted images were acquired with a 1-mm slice thickness, a FOV of 17 × 17 mm² and a matrix size of 64 × 64, yielding a spatial resolution of 0.27 × 0.27 mm².

Fluorescence microscopy of brain sections. Following in vivo MRI studies, mice were anesthetized (75 mg kg^{−1} ketamine, 1 mg kg^{−1} dexmedetomidine in 0.9% saline) and perfused transcardially with 10 mM PBS. Mice brains were then carefully removed and fixed with a 2.5% paraformaldehyde (Santa Cruz Biotechnology, catalog no. sc-281692) solution (wt/vol) for 24 h, followed by their submersion in a 30% (wt/vol.) sucrose solution (in PBS) for 24–48 h for cryogenic preservation. Brains were washed with PBS to remove any sucrose solution excess, and immediately frozen on dry ice and preserved at −80°C. Excised brains were cut into 40-μm-thick slices using dedicated cryotome. The appropriate slices were mounted on microscope slides and imaged using an inverted Leica DMI8 wide-field fluorescent microscope. Consecutive tile stitching with a 10% spatial overlap, according to Leica image analysis software, was generated to obtain complete coverage of the brain slices' FOV. All fluorescent images were analyzed and processed using FIJI software³⁵. HSV1-TK_7B-mCherry and Dm-dNK_7C-GFP expression levels in the brains of the examined mice were imaged using λ_{excitation} = 590 nm, λ_{emission} = 610 nm for mCherry detection; λ_{excitation} = 400 nm, λ_{emission} = 510 nm for GFP detection.

Data analysis and graphic presentation. All the graphical data presented in the paper were analyzed and generated using Prism v.7 software (Graphpad).

Statistical analysis. All numerical results are presented in the form of mean ± s.e.m. and unpaired Student's *t*-test was used for statistical comparison and significance evaluations (as noted in the figure captions). All statistical evaluations were performed using two-tailed analysis unless noted differently in the figure caption.

Reporting Summary. Further information on research design is available in the Nature Research Reporting Summary linked to this article.

Data availability

The datasets generated in this study are available at <https://doi.org/10.5281/zenodo.5594956>. Source data are provided with this paper.

Code availability

The PROSS-design algorithm is available for noncommercial use through a webserver online (<http://pross.weizmann.ac.il>). The MATLAB scripts used for processing the CEST data are available at <http://godzilla.kennedykrieger.org/CEST/>. The Python code and the relevant data used for CEST simulations can be found at <https://github.com/nirbhayyadav/NBT-RA51532A>.

References

35. Schneider, C. A., Rasband, W. S. & Eliceiri, K. W. NIH Image to ImageJ: 25 years of image analysis. *Nat. Methods* **9**, 671–675 (2012).
36. Frey, S. & Gorlich, D. A new set of highly efficient, tag-cleaving proteases for purifying recombinant proteins. *J. Chromatogr. A* **1337**, 95–105 (2014).
37. Peleg, Y. & Unger, T. Application of high-throughput methodologies to the expression of recombinant proteins in *E. coli*. *Methods Mol. Biol.* **426**, 197–208 (2008).
38. Unger, T., Jacobovitch, Y., Dantes, A., Bernheim, R. & Peleg, Y. Applications of the restriction free (RF) cloning procedure for molecular manipulations and protein expression. *J. Struct. Biol.* **172**, 34–44 (2010).
39. Lee, J. S. et al. Urea cycle dysregulation generates clinically relevant genomic and biochemical signatures. *Cell* **174**, 1559–1570 e1522 (2018).
40. Kim, M., Gillen, J., Landman, B. A., Zhou, J. & van Zijl, P. C. M. Water saturation shift referencing (WASSR) for chemical exchange saturation transfer (CEST) experiments. *Magn. Reson. Med.* **61**, 1441–1450 (2009).
41. Liu, G., Song, X., Chan, K. W. & McMahon, M. T. Nuts and bolts of chemical exchange saturation transfer MRI. *NMR Biomed.* **26**, 810–828 (2013).
42. Liu, G., Li, Y. & Pagel, M. D. Design and characterization of a new irreversible responsive PARACEST MRI contrast agent that detects nitric oxide. *Magn. Reson. Med.* **58**, 1249–1256 (2007).
43. Morales, J. L. & Nocedal, J. Remark on 'Algorithm 778: L-BFGS-B: Fortran subroutines for large-scale bound constrained optimization'. *ACM Trans. Math. Softw.* **38**, 1–4 (2011).
44. Woessner, D. E., Zhang, S., Merritt, M. E. & Sherry, A. D. Numerical solution of the Bloch equations provides insights into the optimum design of PARACEST agents for MRI. *Magn. Reson. Med.* **53**, 790–799 (2005).
45. Glunde, K., Jie, C. & Bhujwala, Z. M. Molecular causes of the aberrant choline phospholipid metabolism in breast cancer. *Cancer Res.* **64**, 4270–4276 (2004).

Acknowledgements

This project received funding from the European Research Council under the European Union's Horizon 2020 research and innovation program (grant agreement nos. 677715 and 815379 to A.B.-S. and S.J.F., respectively) and by a charitable donation in memory of Sam Switzer (to S.J.F.).

Author contributions

H.A.-A. and A.B.-S. designed the study. O.K. and S.J.F. performed and analyzed computational design calculations. N.D.T. synthesized 5-MDHT. H.A.-A. carried out all experiments, including cloning, transfections, cell-line establishment, western blots, FACS and in vivo CEST experiments, tumor inoculations, AAV viral infections and histology. Y.P., O.D. and S.A. performed bacterial protein expression, purification and crystallization. A.B. and T.M. developed optimized and performed LC-MS experiments. H.A.-A. and L.A. performed NMR experiments and H.A.-A. and T.H. performed in vitro CEST experiments. N.N.Y. performed CEST simulations and postprocessing of in vitro CEST data using Lorentzian line fitting approach. H.A.-A. and A.B.-S. analyzed the data and wrote the paper with input from O.K. and S.J.F.

Competing interests

The authors declare no competing interests.

Additional information

Supplementary information The online version contains supplementary material available at <https://doi.org/10.1038/s41587-021-01162-5>.

Correspondence and requests for materials should be addressed to Amnon Bar-Shir.

Nature Biotechnology thanks Kevin Brindle, Franz Schilling and the other, anonymous, reviewer(s) for their contribution to the peer review of this work.

Reprints and permissions information is available at www.nature.com/reprints.

Reporting Summary

Nature Research wishes to improve the reproducibility of the work that we publish. This form provides structure for consistency and transparency in reporting. For further information on Nature Research policies, see our [Editorial Policies](#) and the [Editorial Policy Checklist](#).

Statistics

For all statistical analyses, confirm that the following items are present in the figure legend, table legend, main text, or Methods section.

- | | |
|-------------------------------------|--|
| n/a | Confirmed |
| <input type="checkbox"/> | <input checked="" type="checkbox"/> The exact sample size (n) for each experimental group/condition, given as a discrete number and unit of measurement |
| <input type="checkbox"/> | <input checked="" type="checkbox"/> A statement on whether measurements were taken from distinct samples or whether the same sample was measured repeatedly |
| <input type="checkbox"/> | <input checked="" type="checkbox"/> The statistical test(s) used AND whether they are one- or two-sided
<i>Only common tests should be described solely by name; describe more complex techniques in the Methods section.</i> |
| <input checked="" type="checkbox"/> | <input type="checkbox"/> A description of all covariates tested |
| <input checked="" type="checkbox"/> | <input type="checkbox"/> A description of any assumptions or corrections, such as tests of normality and adjustment for multiple comparisons |
| <input type="checkbox"/> | <input checked="" type="checkbox"/> A full description of the statistical parameters including central tendency (e.g. means) or other basic estimates (e.g. regression coefficient) AND variation (e.g. standard deviation) or associated estimates of uncertainty (e.g. confidence intervals) |
| <input type="checkbox"/> | <input checked="" type="checkbox"/> For null hypothesis testing, the test statistic (e.g. F , t , r) with confidence intervals, effect sizes, degrees of freedom and P value noted
<i>Give P values as exact values whenever suitable.</i> |
| <input checked="" type="checkbox"/> | <input type="checkbox"/> For Bayesian analysis, information on the choice of priors and Markov chain Monte Carlo settings |
| <input checked="" type="checkbox"/> | <input type="checkbox"/> For hierarchical and complex designs, identification of the appropriate level for tests and full reporting of outcomes |
| <input checked="" type="checkbox"/> | <input type="checkbox"/> Estimates of effect sizes (e.g. Cohen's d , Pearson's r), indicating how they were calculated |

Our web collection on [statistics for biologists](#) contains articles on many of the points above.

Software and code

Policy information about [availability of computer code](#)

Data collection

FACS studies was acquired using a LSRII cell analyzer flow cytometer (BD Biosciences) running FACSDIVA 8.0.1 software (BD Biosciences). m-Cherry and GFP positive stable cell lines were generated by cell sorting using a FACS Aria cell sorter (BD Biosciences). Western blot data was acquired using ChemiDocTM Imaging System (Bio-Rad). 15.2 T MRI scanner (Biospec, Bruker, Germany) running Paravision 6.0.1 software was used to acquire all the MR imaging data. NMR studies were acquired using a vertical 500 MHz NMR spectrometer (Bruker, Germany). Inverted Leica DMI8 wide-field fluorescent microscope for fluorescent images capture. Crystals structure was obtained using the hanging-drop vapor-diffusion method with a Mosquito robot (TTP Lab Tech). All data sets were collected at 100K on a single crystal on in-house RIGAKU RU-H3R.

Data analysis

Computational display of ligands over protein models were generated using pair fitting in PyMol 2.4.0 software. FACS data was processed using FlowJo™ Software Version 10 (Tree Star, Ashland, OR). MassLynx and TargetLynx software (version 4.2, Waters) were employed to acquire and analyze LC/MS data. CEST MRI data was processed using custom-written scripts in MATLAB (R2014a, Mathworks) which are available through <http://godzilla.kennedykrieger.org/CEST/>. Lorentzian line shape fitting of CEST-MRI data was applied to generated simulated substrate CEST data using the L-BFGS-B function minimization algorithm in Python2.7. High resolution NMR data was processed using Topspin 3.6.2 (Bruker, Germany). Image analysis (Fluorescent images, Western blots, and MR images) was performed using Fiji 2.1.0/1.53c (ImageJ). All the graphical data presented in the manuscript were analyzed and generated using either Excel 2016 (Microsoft) or Prism V7 (Graphpad) software. Illustration were made using Illustrator CC 25.4.1 (Adobe). Diffraction images of Dm-dNK_7C crystals were indexed and integrated using the Mosflm program⁷, and the integrated reflections were scaled using the SCALA program.

Structure factor amplitudes were calculated using TRUNCATE from the CCP4 program suite. The crystal structure was solved by molecular replacement with the program PHASER. All steps of atomic refinement of protein structures were carried out with the CCP4/REFMAC5 program and by Phenix refine. The models were built into 2mFobs - DFcalc, and mFobs - DFcalc maps by using the COOT program.

For manuscripts utilizing custom algorithms or software that are central to the research but not yet described in published literature, software must be made available to editors and reviewers. We strongly encourage code deposition in a community repository (e.g. GitHub). See the Nature Research [guidelines for submitting code & software](#) for further information.

Data

Policy information about [availability of data](#)

All manuscripts must include a [data availability statement](#). This statement should provide the following information, where applicable:

- Accession codes, unique identifiers, or web links for publicly available datasets
- A list of figures that have associated raw data
- A description of any restrictions on data availability

The PROSS-design algorithm is available for noncommercial use through a web server online (<http://pross.weizmann.ac.il>).

The MatLab scripts used for processing the CEST data are available through <http://godzilla.kennedykrieger.org/CEST/>

The Python code and the relevant data used for CEST simulations can be found at <https://github.com/nirbhayyadav/NBT-RA51532A>

PDB codes: 2VP4, 2VP5, 2VPP, 2VPO, 6YBH

Raw data for Figures 1, 2 and 3 is available at <https://doi.org/10.5281/zenodo.5594956>

Field-specific reporting

Please select the one below that is the best fit for your research. If you are not sure, read the appropriate sections before making your selection.

☒ Life sciences ☐ Behavioural & social sciences ☐ Ecological, evolutionary & environmental sciences

For a reference copy of the document with all sections, see [nature.com/documents/nr-reporting-summary-flat.pdf](https://www.nature.com/documents/nr-reporting-summary-flat.pdf)

Life sciences study design

All studies must disclose on these points even when the disclosure is negative.

Sample size	Sample sizes (n>3) were determined based on prior literature and best practices in the field (J Am Chem Soc. 2013: 135, 1617-1624; Magn Reson Med. 2018: 79, 1010-1019). Therefore, no statistical methods were used to predetermine sample size.
Data exclusions	No data was excluded from the analysis.
Replication	All replicates are reported in the manuscript, and were all used for the analyses described in the figures captions. All attempts at replication were successful.
Randomization	In vivo MRI experiments were performed on 2-3 animals per day. For the CHO tumor model, animals were injected with transgenic cells a week prior the planned experiment (1-2 animals at the time). In order to test the reliability and robustness of the approach, two subjects bearing two tumors (CHO-Dm-dNK_7C-GFP and CHO-HSV1-TK_7B-mCherry) were imaged after the injection of only one reporter probe (pDC or 5-MDHT) rather than with their mixtures. For the AAV-model, animals were injected with AAV-virus two weeks prior the planned experiment (1-2 animals at the time).
Blinding	Not relevant to this study. No blinding was used throughout experiments. All data collected was quantifiable and data processing and analyses were performed in the same way as mentioned in the text and therefore blinding would not change any bias in the acquired data.

Reporting for specific materials, systems and methods

We require information from authors about some types of materials, experimental systems and methods used in many studies. Here, indicate whether each material, system or method listed is relevant to your study. If you are not sure if a list item applies to your research, read the appropriate section before selecting a response.

Materials & experimental systems

n/a	Involved in the study
<input type="checkbox"/>	<input checked="" type="checkbox"/> Antibodies
<input type="checkbox"/>	<input checked="" type="checkbox"/> Eukaryotic cell lines
<input checked="" type="checkbox"/>	<input type="checkbox"/> Palaeontology and archaeology
<input type="checkbox"/>	<input checked="" type="checkbox"/> Animals and other organisms
<input checked="" type="checkbox"/>	<input type="checkbox"/> Human research participants
<input checked="" type="checkbox"/>	<input type="checkbox"/> Clinical data
<input checked="" type="checkbox"/>	<input type="checkbox"/> Dual use research of concern

Methods

n/a	Involved in the study
<input checked="" type="checkbox"/>	<input type="checkbox"/> ChIP-seq
<input type="checkbox"/>	<input checked="" type="checkbox"/> Flow cytometry
<input type="checkbox"/>	<input checked="" type="checkbox"/> MRI-based neuroimaging

Antibodies

Antibodies used	All antibodies were commercially purchased. Mouse Anti-b-actin (Santa Cruz biotechnology Inc., Dallas, USA; cat. No. sc-69879; 1:10,000 dilution). Mouse anti-tubulin antibodies (Santa Cruz biotechnology Inc., Dallas, USA; cat. No. sc-5286; 1:10,000 dilution). Mouse Anti-V5 (Thermo Fisher Scientific, Waltham, MA, USA; cat. No.: R960-25; 1:5,000 dilution). HRP Rabbit anti mouse Secondary antibody (Santa Cruz biotechnology Inc., Dallas, USA, cat. No.: sc-516102, 1:10,000 dilution).
Validation	Binding specificity of all of the antibodies were validated and stated in the manufacturers' websites. All antibodies used in this study have been used in prior studies and are routinely used in our lab.

Eukaryotic cell lines

Policy information about [cell lines](#)

Cell line source(s)	Human embryonic kidney-293 (HEK-293) were obtained from the tissue culture cell repository unit at the Weizmann Institute of Science, Rehovot, Israel. Chinese hamster ovarian (CHO) cell line were purchased from ATCC (Manassas, Virginia, USA).
Authentication	None of the cell lines were authenticated.
Mycoplasma contamination	All cell lines used in this study were tested negative for Mycoplasma
Commonly misidentified lines (See ICLAC register)	HEK-293 cells were used in this study and are listed as a commonly misidentified with HeLa, which were not included in this study. Nevertheless, it is important to mention here that misidentification of the HEK-293 cells with another cell type would not change by any mean the major conclusions drawn from this study. HEK-293 are commonly used due to their well-established culture techniques including for studies involved the development of transgene expression and studies involved the development of MRI-reporter genes.

Animals and other organisms

Policy information about [studies involving animals](#); [ARRIVE guidelines](#) recommended for reporting animal research

Laboratory animals	8 weeks female immunodeficient Hsd:ATHymic Nude-Foxn1nu mice (Envigo, Israel) were used for the tumor model in vivo 8 weeks female SJL/JCrHsd (Envigo, Israel) were used for the AAV model in vivo. All experiments involving animals were performed following the described experimental protocol approved by the Weizmann Institute of Sciences Animal Care and Use Committee (IACUC approval number- 11850319-2). All animals were kept in a daily controlled room at the Weizmann Institute of Sciences animal facility with a surrounding relative humidity level of 50% \pm 10% and a temperature of 22 \pm 1oC, with a12/12 cycle of dark and light phases.
Wild animals	The study did not involve wild animals.
Field-collected samples	The study did not involve sample collection in the field.
Ethics oversight	All experiments involving animals were performed following the described experimental protocol that was approved by the Weizmann Institute of Sciences Animal Care and Use Committee.

Note that full information on the approval of the study protocol must also be provided in the manuscript.

Flow Cytometry

Plots

Confirm that:

- ☒ The axis labels state the marker and fluorochrome used (e.g. CD4-FITC).
- ☒ The axis scales are clearly visible. Include numbers along axes only for bottom left plot of group (a 'group' is an analysis of identical markers).
- ☒ All plots are contour plots with outliers or pseudocolor plots.
- ☒ A numerical value for number of cells or percentage (with statistics) is provided.

Methodology

Sample preparation	HEK 293 or CHO cells lines were cultured and incubated with the fluorescent studied probe. Following cell incubation, cell were washed twice with cold PBS, dissolved in FACS solution (1% FBS in PBS) then filtered though a 40 micron mesh filter into a FACS analysis tube and subsequently analyzed by FACS . All the cells were kept on ice from the samples preparation until FACS analysi
Instrument	We used flow LSRII (BD Biosciences) cell analyzer running FACSDiva software for FACS studies acquisition.

Software	FlowJo version 10 was used for analysis.
Cell population abundance	FACS sorting was used to sort Dm-dNK_7C-GFP or HSV1-TK_7B-mCherry positive cells in order to establish stable cell lines for tumor inoculation in the in vivo studies (MRI). The abundance of relevant cell populations within post-sort fractions was >90%.
Gating strategy	For pdC accumulation determination gating was used to evaluate positive fluorescent cells population (using UV-fluorescent laser setup of $\lambda_{excitation}=355\text{nm}$ and $\lambda_{emission}=460\text{ nm}$) and set based on negative control cells without the presence of the fluorescent probe (pdC).

☒ Tick this box to confirm that a figure exemplifying the gating strategy is provided in the Supplementary Information.

Magnetic resonance imaging

Experimental design

Design type	Static image
Design specifications	Described in Methods section.
Behavioral performance measures	No behavioral performance was measured.

Acquisition

Imaging type(s)	Structural imaging and chemical exchange saturation prior and following probes administration.
Field strength	15.2 T
Sequence & imaging parameters	Described in Methods section.
Area of acquisition	Brain
Diffusion MRI	<input type="checkbox"/> Used <input checked="" type="checkbox"/> Not used

Preprocessing

Preprocessing software	ParaVision 6.0.1, FIJI-ImageJ, MatLab
Normalization	N/A. All data sets were acquired using the same setup and the same experimental parameters and no data normalization was used.
Normalization template	N/A. Data normalization was not applicable in this study and the use of normalization template was not needed.
Noise and artifact removal	CEST data post-processing was performed on the raw data without noise or artifact removals. Outliers noise removal (FIJI-ImageJ) was applied on the obtained CEST maps using 1 pixel radius.
Volume censoring	Volume censoring was not applied and the CEST data processing was applied on the raw data as they were acquired.

Statistical modeling & inference

Model type and settings	Statistical modeling was not applied
Effect(s) tested	CEST MRI signal was analyzed at different chemical shift in the all brain following probe administration without any task or stimuli applied.
Specify type of analysis:	<input type="checkbox"/> Whole brain <input checked="" type="checkbox"/> ROI-based <input type="checkbox"/> Both
Anatomical location(s)	MRI slices were localized based on the observation of the injection site of either the CHO cells (tumor model) or the AAV (viral infection model).
Statistic type for inference (See Eklund et al. 2016)	Student's t-test.
Correction	No correction was applied

Models & analysis

n/a	Involvement in the study
<input checked="" type="checkbox"/>	<input type="checkbox"/> Functional and/or effective connectivity
<input checked="" type="checkbox"/>	<input type="checkbox"/> Graph analysis
<input checked="" type="checkbox"/>	<input type="checkbox"/> Multivariate modeling or predictive analysis